

See discussions, stats, and author profiles for this publication at: <https://www.researchgate.net/publication/231231515>

In-Plane Epitaxial Growth of Self-Assembled Ge Nanowires on Si Substrates Patterned by a Focused Ion Beam

ARTICLE in CRYSTAL GROWTH & DESIGN · JUNE 2011

Impact Factor: 4.89 · DOI: 10.1021/cg200433r

CITATIONS

12

READS

66

10 AUTHORS, INCLUDING:



I. Berbezier

French National Centre for Scientific Research

177 PUBLICATIONS 2,083 CITATIONS

[SEE PROFILE](#)



Maria Isabel Alonso

Materials Science Institute of Barcelona

141 PUBLICATIONS 2,621 CITATIONS

[SEE PROFILE](#)



Miquel Garriga

Materials Science Institute of Barcelona

130 PUBLICATIONS 3,423 CITATIONS

[SEE PROFILE](#)



Alejandro Goñi

Materials Science Institute of Barcelona

156 PUBLICATIONS 2,443 CITATIONS

[SEE PROFILE](#)

In-Plane Epitaxial Growth of Self-Assembled Ge Nanowires on Si Substrates Patterned by a Focused Ion Beam

I. Carmen Marcus,^{†,‡} Isabelle Berbezier,^{*,‡} Antoine Ronda,[‡] M. Isabel Alonso,^{*,†} Miquel Garriga,[†] Alejandro R. Goñi,^{†,§} Elise Gomes,^{‡,||} Luc Favre,[‡] Anne Delobbe,^{||} and Pierre Sudraud^{||}

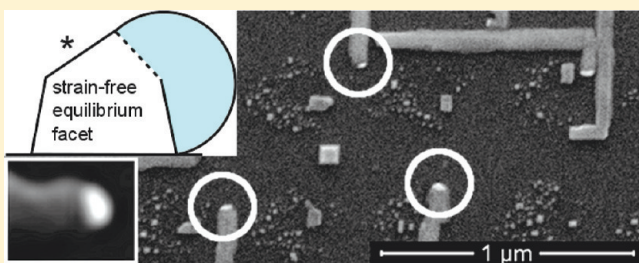
[†]Institut de Ciència de Materials de Barcelona—CSIC, Esfera UAB, 08193 Bellaterra, Spain

[‡]IM2NP, CNRS—Univ. Aix Marseille, Campus St. Jérôme, Case 142, 13397 Marseille Cedex 20, France

[§]ICREA, Passeig Lluís Companys 23, 08010 Barcelona, Spain

^{||}Orsay Physics, 95 Avenue des Monts Auréliens—ZA Saint-Charles, 13710 Fuveau, France

ABSTRACT: We report a novel method for obtaining ordered arrays of self-assembled Ge nanowires (NWs) using Au seed catalysts, with the latter deposited using a focused ion beam (FIB). For this purpose we apply a three-step process involving first FIB nanopatterning, a second step of AuSi seed formation during UHV annealing, and third the nucleation and growth of Ge NWs by combining molecular-beam epitaxy (MBE) and the vapor–liquid–solid (VLS) process. We show that FIB allows for the local implantation of Au in the areas impacted by the ion beam; the implanted Au evolves during annealing into AuSi clusters, serving as nucleation seeds for the nucleation and growth of Ge NWs. We thus prove that FIB with gold ions is a successful method to obtain gold-catalyzed self-assembled nanowires. We obtain Ge NWs of homogeneous dimensions and oriented in-plane along [110] directions, as a consequence of a strain-driven process. Wire kinking is governed by surface morphological features. Based on our experimental results, we elaborate on the general mechanisms of MBE growth of quantum wires under epitaxial strain, which we exemplify for Ge NWs on Si(001) but hold for many other lattice-mismatched semiconductor material combinations.



1. INTRODUCTION

A wide range of photovoltaic devices employing different active semiconductors have been developed during the past decade, to compete with less expensive materials, which generally produce lower efficiencies. The issue is to optimize the optical/electrical properties of such devices using new functionalities and smaller amounts of materials in order to implement third generation solar cell approaches that lift up their efficiencies. The two main strategies followed so far with nanostructured solar cells are to increase (a) the number of energy levels harvested and (b) the electron generation and transport by multiple carrier pair generation per high energy photon or single carrier pair generation with multiple low energy photons. Technologies based on semiconductor quantum devices are actively discussed in the literature.^{1–3} They are foreseen to potentially improve the efficiency of solar cells by enhancing photon absorption and electron production and transport. In particular, quantum-dot and quantum-wire-based solar cells should offer a way to exceed the thermodynamic one-junction Shockley–Queisser efficiency limit,⁴ since such nanostructured materials can be superimposed on advanced-concept solar cell structures.

To date, various methods to fabricate semiconductor nanowires (NWs) have been reported, such as vapor–liquid–solid (VLS) growth,^{5–7} solid–liquid–solid (SLS) growth,⁸ oxide-assisted growth,⁹ vapor–solid–solid (VSS) growth,^{10–12} the electroless metal deposition (EMD) method,^{13,14} and others.^{15–17}

Despite the large number of studies reporting the modifications of the NWs diameter by using different ambient gases,^{18,19} ambient pressure,^{20,21} and catalyst clusters of homogeneous size,^{22,23} most of the processes developed often resulted in NWs with inhomogeneous diameters and lengths and randomly oriented and positioned.

Regarding the Si NWs, they are usually grown by the vapor–liquid–solid (VLS) mechanism using different catalysts.^{11,24–26} Among them, gold was found to be the best candidate, to control Si NW growth due to the formation of a AuSi alloy with low eutectic point.²⁷ In contrast, Ge NWs received much less attention as compared to the Si ones. However, compared to silicon, germanium provides better mobility, smaller bandgap, and a larger exciton Bohr radius, which provides quantum confinement effects at larger nanowire sizes.²⁸ Even though elementary processes of NWs growth using the VLS mechanism have been investigated,^{29–31} a complete understanding of the driving force controlling the shape is still missing. Moreover, from a more technological point of view, the self-assembly of NWs should be largely improved to expect any possible use in devices; in particular, the control of the position and of the size distribution are still lacking.

Received: April 7, 2011

Revised: May 20, 2011

Published: May 27, 2011

The aim of the present study is to develop a method to obtain NWs using Au seed catalysts and to control the size and the density of NWs by varying the Au nanocluster features. For this purpose, we apply mass-filtered focused ion beam (FIB) direct writing using Au^{2+} ions to form a bidimensional array of Au nanoclusters. We have developed a three-step process involving a first step of nanopatterning using an ultrahigh resolution focused ion beam (HR-FIB), a second step of AuSi formation during UHV annealing, and a third step of Ge NW nucleation and growth by solid-source molecular-beam epitaxy (MBE) using the VLS process. Here we demonstrate that HR-FIB allows for the local implantation of Au in the areas impacted by the ion beam; the implanted Au evolves during annealing into AuSi clusters that can be subsequently used as nucleation seeds for the growth of Ge NWs. We focus on the case of growth on Si(001) substrates, and based on our experimental results, we analyze the elementary mechanisms of nanowire growth under epitaxial strain.

2. EXPERIMENTAL METHODS

The developed experimental procedure consists of three steps: (1) FIB nanopatterning; (2) AuSi clusters formation, and (3) Ge nanowire nucleation and growth. Patterning experiments have been carried out in a Tescan LYRA1 XMH dual-beam workstation operating at 30 keV. This dual beam is equipped with a mass-filtered ultrahigh resolution focused ion beam COBRA-FIB from Orsay Physics, which has an ultimate resolution of 5 nm (using Ga^+ ions). For this work, the liquid metal alloy ion source (LMAIS) used is the eutectic AuSi alloy heated at 380 °C. The patterns were performed with Au^{2+} ions selected with the mass filter (3.27×10^{-25} kg) using a mass selection aperture of 20 μm . Under these conditions, the FIB resolution reaches ~15 nm. The combination of beam size and of the large Au^{2+} ions (about 1.2 Å in size) limits the minimum lateral dimensions of the patterns to a diameter of ~50 nm.

Several arrays of nanopatterns were milled using FIB with Au^{2+} ions. The nanopattern size, depth, and aspect ratio were changed by varying the ion beam current, ion dose, dwell time, and spot size. The amount of Au^{2+} ions that irradiate the sample (exposure) depends on each one of these parameters. Different exposures were tested by varying the beam current from 1 to 60 pA. Different ion beam conditions were obtained by changing the probe aperture from 10 to 50 μm . The exposure doses were also varied by changing the writing time between 5 and 200 ms. The 2D periodic arrays of patterns were performed following two different scanning exposure procedures either in series or in parallel. In both situations there was no beam blanking between two consecutive impacts. Usually, the size of the patterned area was $25 \times 25 \mu\text{m}^2$ and the total patterning time varied between 30 s and 20 min. The periodicity of the patterned features was chosen to be 500 nm. Depending on the ion doses, the depth of maximum implantation of Au^{2+} in the Si substrates varied from 1 nm for a dose of 17×10^{-4} C/cm² to 42 nm for a dose of 184×10^{-4} C/cm². The substrates patterned were Si(001) p type doped with boron at 5×10^{17} cm⁻³, and occasionally, we also used Si(111). The sputtering angle between the ion beam and the Si substrate surface was kept constant at 90° (normal incidence).

During pattern preparation, the incident Au ions are locally implanted at the subsurface of the substrate areas and nearby the patterns. This local implantation was used, in a second step, to form the AuSi clusters during a high temperature annealing. Various annealing temperatures were investigated, especially in a range of 200 °C around the eutectic temperature (380 °C for AuSi) and also higher, up to 850 °C. After the FIB patterning, the substrates were systematically ex-situ cleaned by a Shiraki modified process in a clean room atmosphere to produce an H-terminated surface. They were then immediately transferred into the molecular beam epitaxy (MBE) UHV growth chamber and in-situ flashed using a slow thermal ramp from room temperature to the

annealing temperature. The formation of AuSi clusters was investigated at various annealing temperatures and times (UHV residual pressure $\sim 10^{-10}$ Torr). After annealing, the AuSi clusters were systematically observed ex-situ by atomic force microscopy (AFM) in air and scanning electron microscopy (SEM).

The third step of the process consists of Ge deposition on the samples where AuSi clusters have been formed. Based on the previous annealing experiments, we selected a temperature of 550 °C. During this step, the samples were annealed and kept on the sample holder of the UHV growth chamber for growth at the same temperature (550 °C). This temperature was reached in 20 min, followed by 15 min of annealing and deposition of 2–12 nm of Ge from an effusion cell at a rate of $\sim 3.5 \times 10^{-2}$ nm/s. The uniformity of the Ge thickness was ensured by the continuous rotation of the substrate. After deposition, the temperature was immediately lowered following a ramp of 20 °C/min until below 250 °C. After the different stages of the process, systematic observations of the samples were performed ex-situ by AFM in air and SEM.

3. RESULTS AND DISCUSSION

3.1. AuSi Cluster Formation Using FIB with Au^{2+} Ions. We first investigated the formation of AuSi clusters by a LMAIS HR-FIB patterning process using Au^{2+} ions. The aim was to precisely control the size and the position of the AuSi clusters. For this purpose, the Si(001) substrates were bombarded by Au^{2+} ions under various FIB exposure conditions. We first varied the ion fluxes in order to modify the balance between erosion and implantation. When reducing the ion flux from 4.09×10^{15} to 0.052×10^{15} ions/cm²/s (source apertures are 50 and 20 μm , respectively), the morphology of the patterns switched from holes to mounds. AFM views of the patterned areas after FIB scans under these conditions are presented in Figure 1. We can clearly see the change of the patterns from holes to mounds from Figure 1a to 1b. A larger scale AFM image and a line profile (inset) of the border of the patterned area in the latter situation are presented in Figure 1c. They both show that the surface level of the mounds is higher than those of the unpatterned substrate. This proves that mounds have been formed onto the surface due to a larger quantity of implanted ions as compared to the eroded matter under these experimental conditions.

We then investigated in these two regimes the morphological evolution of the patterns with the two different source apertures. In the regime of mound formation, using a 20 μm source aperture, the size of the mounds can be tuned by varying the ion beam intensity, which depends on the focused spot size, as illustrated in Figure 2. As an example, we present here the AFM images of the mounds formed for spot sizes of $\varphi = 40$ and 20 nm (parts a and b, respectively, of Figure 2). With the rest of the parameters fixed, the ion beam size is proportional to φ , and thus, we observe a linear increase of the mean diameter of the mounds with focused spot size (Figure 2c), which can be directly related to an increasing ratio between the eroded matter and the implanted ions.

At higher ion beam intensities, under the conditions of hole formation (using a 50 μm source aperture; see Figure 3a), we also investigated the morphological evolution of the holes with the exposure. We observed a linear increase of the aspect ratio of the holes with the ion dose, corresponding to a linear increase of the depth at a constant lateral diameter (see Figure 3b).

The various morphological situations described above were used to test the second step of the process i.e., the AuSi cluster formation during annealing. This step requires, first, a large quantity of Au locally implanted near the patterns and, second,

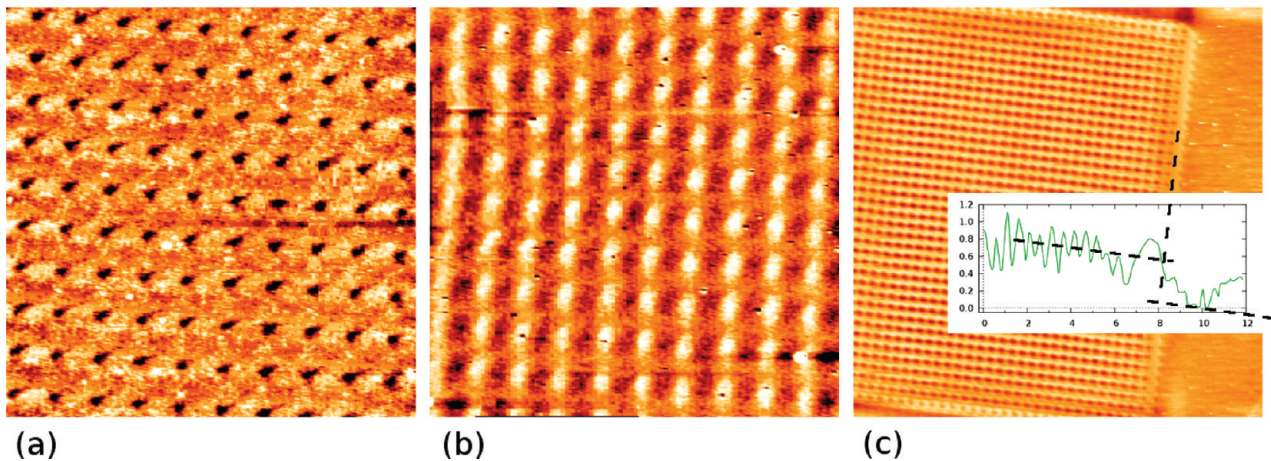


Figure 1. AFM images of the patterns obtained under different FIB irradiation conditions. The source aperture was varied between (a) $50\text{ }\mu\text{m}$ and (b) $20\text{ }\mu\text{m}$. In part c, a larger scale image is presented, revealing the outgrowth over the patterned area. The scan area for parts a and b is $5 \times 5\text{ }\mu\text{m}^2$, and that for part c is $20 \times 20\text{ }\mu\text{m}^2$. The focused spot size in both cases was 50 nm.

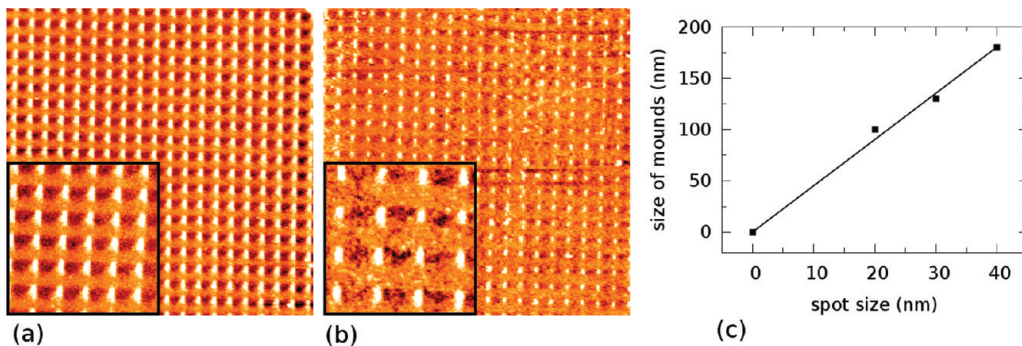


Figure 2. AFM images of mounds formed during FIB experiments at a $20\text{ }\mu\text{m}$ source aperture, using beam sizes corresponding to a focused spot size of (a) 40 and (b) 20 nm. The graph in part c gives the morphological evolution of mounds with the spot size. The imaged area for parts a and b is $10 \times 10\text{ }\mu\text{m}^2$, inset a is $3 \times 3\text{ }\mu\text{m}^2$, and inset b is $2 \times 2\text{ }\mu\text{m}^2$.

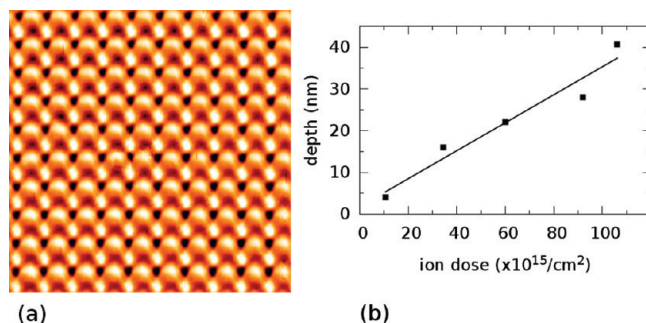


Figure 3. (a) AFM image of a hole pattern formed during FIB experiments using a spot size of 50 nm (image size $5 \times 5\text{ }\mu\text{m}^2$). (b) Hole depth as a function of ion dose.

the segregation/diffusion of Au into crystalline clusters. We investigated the influence of annealing temperature and time on the formation of AuSi crystalline clusters in the two situations reported above: when patterns consist of mounds and when they consist of holes. The annealings were performed in the UHV growth chamber of the MBE machine for different times between 15 and 30 min and for temperatures ranging from 400 to 850 °C. At these temperatures, the thermodynamically stable AuSi

eutectic phase is expected to form liquid nanodroplets at the Si surface.²⁷ After annealing, the samples are cooled to room temperature and they are systematically observed by AFM in air and SEM.

For the samples patterned with mounds, irrespective of the annealing conditions, we systematically observed the total flattening and disappearance of mounds after annealing. It was not possible to observe any formation of AuSi clusters in these cases. We attributed this behavior to an extremely low concentration of gold under these “soft” sputtering conditions.

For the samples patterned with holes, we observed different evolutions depending on the annealing temperature (T_A). For $T_A \geq 650\text{ }^\circ\text{C}$, the patterns with hole depth below 3 nm flatten and disappear (as observed in the case of mounds). For $T_A \leq 450\text{ }^\circ\text{C}$, the patterns remain unchanged and there is no visible formation of crystalline clusters. For $450\text{ }^\circ\text{C} \leq T_A \leq 650\text{ }^\circ\text{C}$, AuSi clusters formed around the holes on the patterned areas. The AuSi cluster formation was followed after successive annealings of 30 min at 550 °C. A large scale image of the pattern morphology after two successive annealings is presented in Figure 4a. The AFM images of the patterns reveal the formation of a large number of ultrasmall clusters in the FIB holes and their surroundings (Figure 4b), which are identified by backscattering scanning electron images (BS-SEM) as Au rich clusters (Figure 4c). We observe an increase of

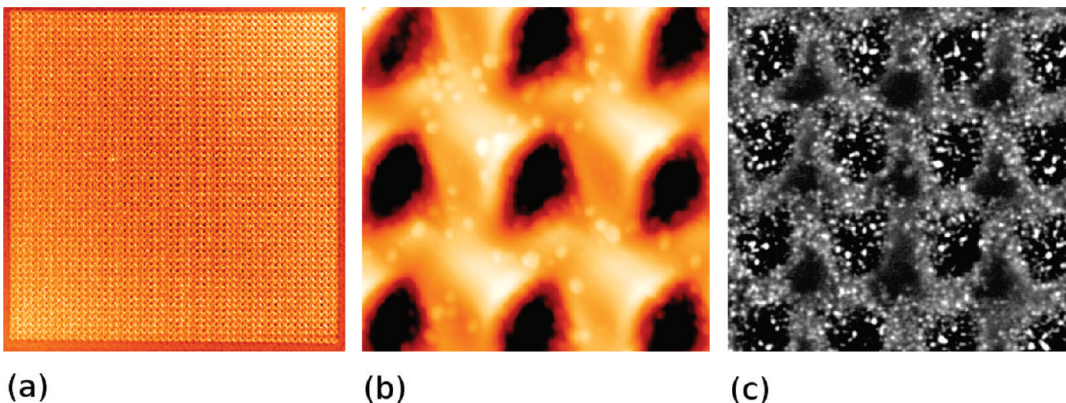


Figure 4. (a) Large scale AFM image of a patterned area after two successive annealings at 550 °C ($20 \times 20 \mu\text{m}^2$ scan); (b) AFM image of the clusters formed around the patterns at $I_{\text{Au}} = 0.0352 \text{ A}/\text{cm}^2$ (scan size $1.5 \times 1.5 \mu\text{m}^2$); (c) BS-SEM image evidencing the presence of Au in the clusters (light areas correspond to Au rich areas). Here clusters formed at $I_{\text{Au}} = 0.1747 \text{ A}/\text{cm}^2$ (scan size $2 \times 2 \mu\text{m}^2$).

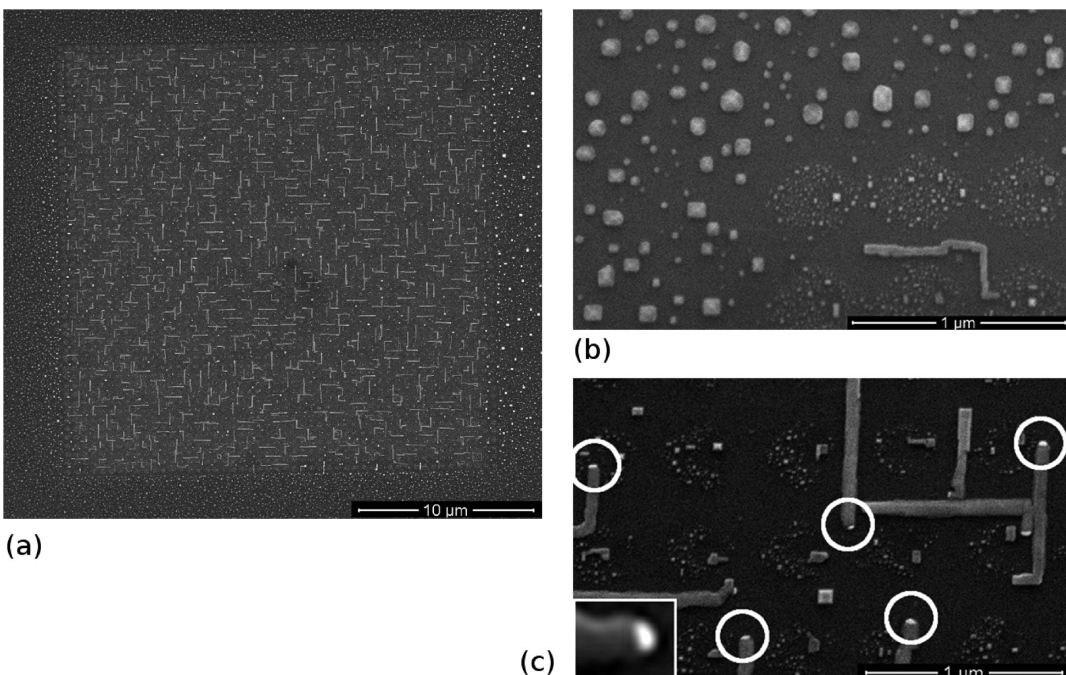


Figure 5. (a) Large scale SEM image of the patterned and unpatterned area; (b) SEM image showing the bimodal distribution of “hut” and “dome” islands on the unpatterned area and a Ge NW on a patterned area (lower right corner); (c) BS-SEM image of Au rich clusters at the tip of NWs; the inset shows a higher magnification image of the cluster.

the lateral distribution and density of clusters with the ion beam intensity (I_{Au}): The larger is I_{Au} , the broader is the lateral cluster distribution and the larger is the density (an example of this evolution is presented in Figure 4b and c, where I_{Au} was varied between 0.0352 and 0.1747 A/cm^2).

3.2. Ge Nanowire Growth on a Si(001) Substrate. In this part, we investigate the growth of Ge nanowires (NWs) on the AuSi clusters fabricated by the FIB patterning process described in the previous part. We followed the strategy developed in the literature using the experimental conditions described above, similar to those reported for the solid-source MBE growth of Si/Ge NWs on Si(111) using AuSi clusters as catalyst seeds.^{23,32} The aim of the present study is to investigate the formation of Ge NWs on Si(001) and the influence of the cluster density on the morphological evolution of NWs. Eight areas of $25 \times 25 \mu\text{m}^2$

were patterned on every Si substrate using ion doses varying between 1.0×10^{16} and 1.1×10^{17} ions/ cm^2 (doses from 1.7×10^{-3} to $1.8 \times 10^{-2} \text{ C}/\text{cm}^2$). Subsequently to the annealing of the patterned substrate, 2–12 nm layer equivalent thicknesses of Ge were deposited by solid source MBE. The SEM observations of the surface show the formation of NWs lying on the Si(001) surface on the patterned areas. These areas are easily distinguished from the unpatterned ones, where only 3D Ge islands were grown under the same deposition conditions (Figure 5a and b). We checked that these 3D islands present the shapes commonly observed in the literature with a bimodal distribution of “huts” and “domes”, as can be seen in Figure 5b.³³

The obtained NWs have approximately trapezoidal sections and a mean aspect ratio about 0.05 with a section square root of about 50 nm and a length of around 1 μm (Figure 5c). BS-SEM

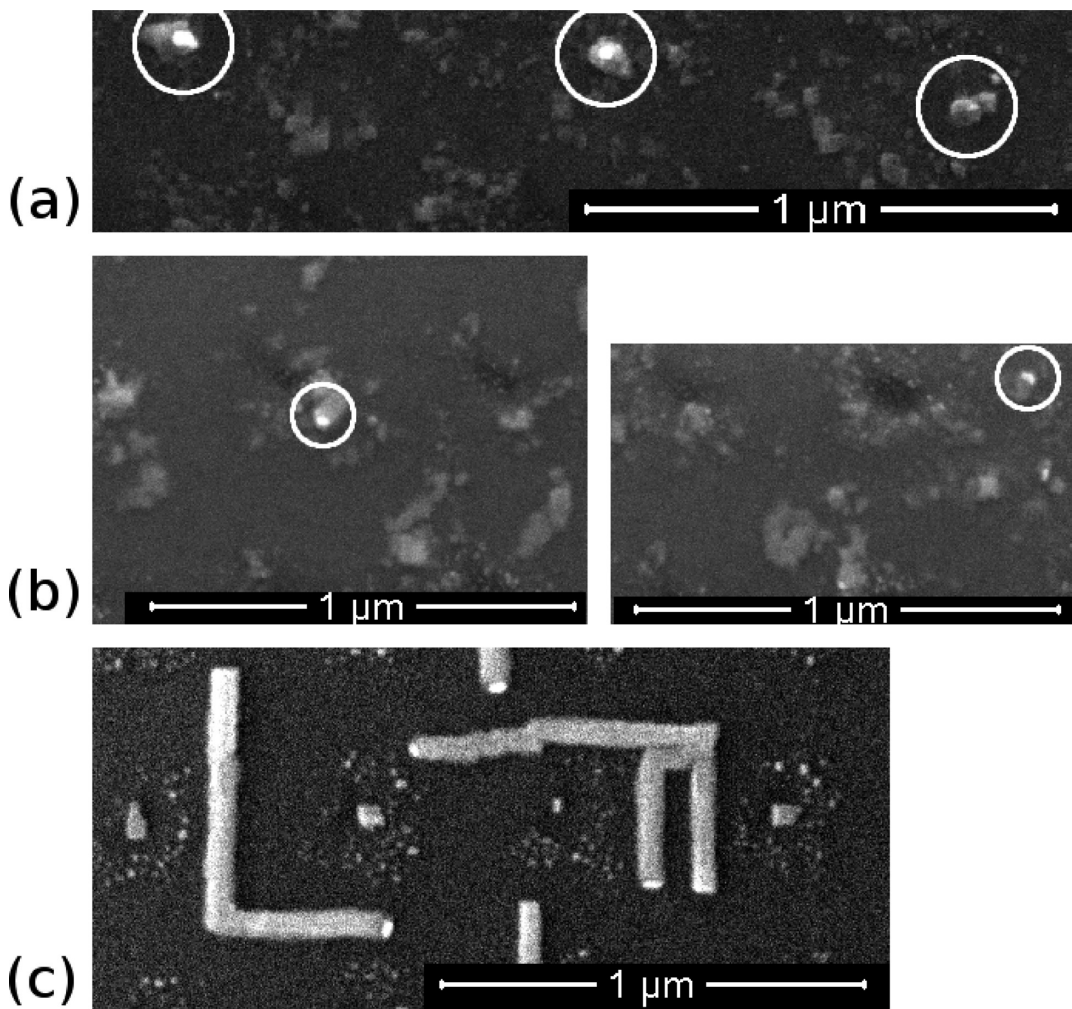


Figure 6. (a) BS-SEM image of the first nucleation stage on the Au rich clusters with NW growth along [001]; (b) SEM images of the second growth stage misoriented from [001]; (c) SEM image of the NWs at the end of the growth process along the [110] directions parallel to the substrate.

observations reveal the presence of Au rich particles at the tip of every NW; these nanoparticles more or less fit the transversal size of the NWs. One can also note that the NWs are all oriented along the {110} directions, even if the NWs present kinks and rotations from one direction to another. Despite the lack of large scale ordering that was expected when patterning the substrate, it is nevertheless clear from Figure 5 that all the NWs nucleate close to the patterns in the areas where AuSi clusters are observed.

A deeper investigation of the NW formation at different growth stages evidences, first, the nucleation of Ge nanostructures at AuSi clusters, accompanied with the initial NW growth almost perpendicular to the surface, up to a critical length (Figure 6a), second, the kinking of NWs (Figure 6b), and third, their crawling on the substrate (Figure 6c). Under different experimental conditions, it was shown that a continuous tapering of the nanowire pedestal could be produced, with a pedestal becoming so narrow that the catalyst rolls off, producing the crawling of the nanowire along the substrate.^{34,35}

To address this growth mechanism of Ge NWs along the substrate, we have to consider the dynamical evolution of NW growth. It was reported that the wire growth is controlled by the dynamical evolution of the trijunction between solid (Ge in our case), vapor, and liquid (AuSi).^{36,37} The liquid–solid (L–S)

kinetics was expressed by Schwarz et al.³⁶ as

$$\nu_s = \alpha_{ls}(\mu_l - \mu_s) \quad (1)$$

where ν_s is the local growth velocity of the solid, α_{ls} is a kinetic rate coefficient taken as nonzero only at the L–S interface, μ_s and μ_l are the chemical potentials of the solid and liquid, respectively, and μ_s was expressed as

$$\mu_s = \Omega_s \left[\kappa\gamma + \kappa \frac{\partial^2\gamma}{\partial n^2} + p + C(\kappa) \right] \quad (2)$$

where $\kappa\gamma$ is the Gibbs term, generalized with the second term ($\kappa(\partial^2\gamma)/(\partial n^2)$) to an orientation-dependent interface energy, with γ changing over the interface following a step function: $\gamma = \gamma_{ls}\Theta_l + \gamma_{vs}(1 - \Theta_l)$, where γ_{ls} and γ_{vs} are the orientation-dependent interfacial energies between the liquid and the solid, and the vapor and the solid, respectively, and Θ_l is a step function representing the pressure. The effect of anisotropy in γ is introduced using the simple relationship³⁶

$$\gamma(\hat{n}) \approx \gamma(1 - \varepsilon_n \cos n\theta) \quad (3)$$

Thus, γ_{vs} and γ_{ls} are multiplied by $(1 - \varepsilon_n \cos n\theta)$, where θ gives the local surface orientation, n is the number of facets, and ε_n is an

arbitrary coefficient depending on the surface symmetry. The orientation of the surface is given by its normal vector \hat{n} , $\kappa = -\nabla_s \hat{n}$ is the curvature tensor, \mathbf{p} is the force normal to the surface, and $C(\kappa)$ is a regularization term limiting the sharpness of edges on faceted surfaces.

The term μ_1 was described using a simplified expression:³⁶

$$\mu_1 = \beta(c_l - c_0) + \Omega_l \gamma_{vl} \kappa_l \quad (4)$$

where the first term represents the supersaturation with respect to the equilibrium liquidus concentration and the second term is the Gibbs–Thomson effect of surface tension.

As a consequence, the NW growth described in eq 1 is based, first, on the kinetic term (α_{ls}), which mainly depends on the surface diffusion of atoms, and, second, on $\Delta\mu$, the formation of new facets at the trijunction, which needs the availability of monatomic kinks and steps at the L–S interface. The additional energy requested to form a new facet depends both on the surface energy of the existing flat facet and on the edge energy of this facet (cf. eq 2). These two terms are orientation dependent and described, for instance, following eq 3. Therefore, the NW sidewalls should follow the orientations that minimize μ_s , since μ_1

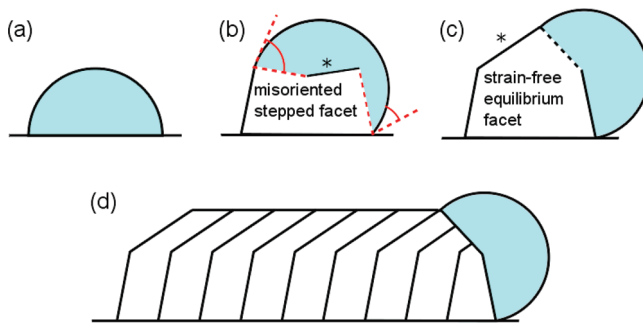


Figure 7. Schematic representation of the three growth stages of the NW starting from (a) the initial state with the AuSi cluster lying at the Si(001) surface. Part b represents the first stage of the NW growth. This stage is characterized by a small pedestal tapering due to the formation of slightly misoriented stepped facets, for instance (105), and the rolling out of the catalyst liquid droplet along the sidewall of the NW. Part c shows the strong kinking of the NW and its morphological change with the onset of strain-free equilibrium facets, for instance (113) and (111). Part d shows the last stage crawling of the NW along the substrate surface and its elongation on the substrate.^{38,39}

is expected to remain almost constant (from eq 4). Under our experimental conditions, we consider that both the kinetic rate of growth (α_{ls}) and μ_1 remain constant, during epitaxial growth of Ge on Si(001) substrate, whereas there is a strong strain-dependent evolution of μ_s due to the change of γ_{vs} and $(\kappa(\partial^2\gamma_{vs})/(\partial h^2))$ in eq 2. In the case of the (001) surface, γ_{vs} increases and $(\kappa(\partial^2\gamma_{vs})/(\partial h^2))$ decreases under compressive epitaxial strain of Ge on Si.³⁸ During the first stage of growth, the NWs are under compressive strain and the energy of [001] step formation becomes low due to a reduction of the step edge energy with strain.³⁸ At the same time, the (001) surface energy (γ_{001}) increases while the surface energy of somewhat misoriented stepped surfaces decreases. In particular, it was demonstrated that 11° off misoriented (105) facets have surface energy γ_{105} lower than γ_{001} .³⁸ This means that (105) facets are apt to nucleate at the expense of biaxially strained (001) facets.^{39,40} Consequently, below a critical deposited thickness (under compressive strain), the nucleation of new facets is favored by the decrease of the step formation with strain, but because of the destabilization of (001), the interface orientation will rotate during growth to follow, for instance, (105) facets. This results in a small tapering of the NWs pedestal and a slight misorientation of the NW sidewalls (Figure 6b). A schematization of the growth process is drawn in Figure 7, starting from the initial state (Figure 7a). The first stage of the NW growth is depicted in Figure 7b. In order to keep the equilibrium value of the contact angle corresponding to the trijunction equilibrium and also for matter conservation, the droplet slightly rolls off the surface and covers the sidewall of the incipient NW.

The second growth stage starts after a critical grown thickness (or NW height) when the strain is relaxed by dislocation nucleation (after ~5 nm NW height, which is larger than in 2D layers). At this point, a strong kinking of the Ge NWs is observed experimentally (Figure 6b), and the strain-free equilibrium facets nucleate on the sidewalls of the NWs, producing a strong change of their growth axis direction (Figure 7c). This morphological change is similar to the “hut” to “dome” islands transformation observed in 2D dimensions, which was explained by an abrupt increase of γ_{105} and of $(\kappa(\partial^2\gamma_{vs})/(\partial h^2))$ due to strain relaxation. The NWs develop similar (113) and (111) sidewalls, like the equilibrium facets of relaxed Ge “domes”, while elastically strained “hut” pyramidal islands have (105) side facets that represent a local minimum of the Ge surface energy under strain.^{38,39}

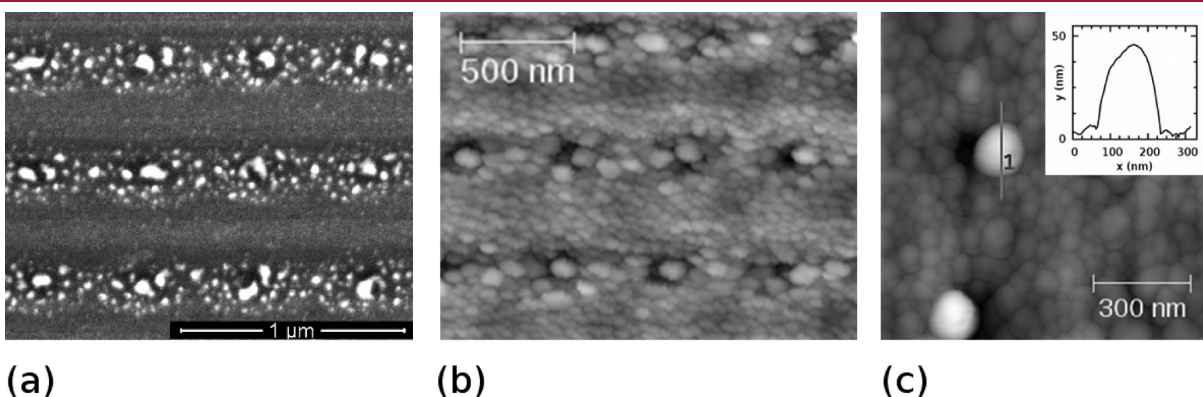


Figure 8. Growth stages of Ge NWs on patterned Si(111). (a) BS-SEM image after depositing 2 nm of Ge. Light areas indicate the presence of Au. (b) AFM image of a similar region after depositing 12 nm of Ge. Ordering effects given by the 500 nm pitch patterned holes are much stronger in this orientation. (c) Detail and profile of one of the observed NWs.

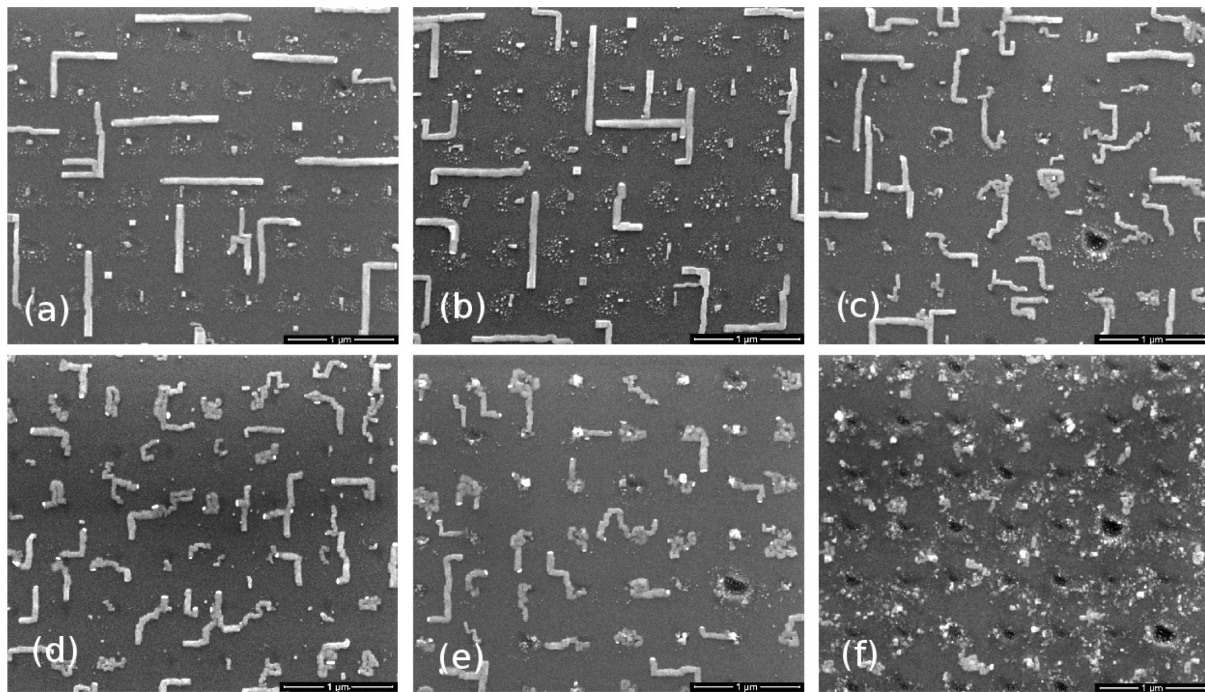


Figure 9. FIB ion dose influence on the NW morphological evolution. Wires grow predominantly along $\langle 110 \rangle$ directions, but the surface roughness acts as a diffusion barrier, producing an increasing waviness until growth is almost hindered. Scale bars are $1 \mu\text{m}$.

During further growth (NW length, about 100 nm in our experiments), the liquid cluster drops in contact with the Si(001) substrate. It rolls on the Si(001) surface, producing the crawling of the NW along the substrate and further growth with its axis parallel to the substrate (Figure 7d), along [110] directions, providing the extension of the (113) and (111) side facets.

These different growth stages, in particular crawling of NWs, were not observed on Si(111)^{41,42} due to the very different anisotropy of the surface energy ($\kappa(\delta^2\gamma_{\text{vs}})/(\delta n^2)$), around [111] compared to [001].⁴³ This is also consistent with the different growth modes of Ge islands on Si(001) and Si(111) observed in the absence of AuSi clusters seeds.^{44,45}

We also performed growth on patterns on Si(111) to confirm that the crawling of NWs that we observed on Si(001) is an intrinsic effect. Indeed, on Si(111) we observe similar growth as in the literature,^{41,42} even for very high Ge coverages up to 12 nm. This is seen in Figure 8: in the initial stage of growth, the Ge NWs grow perpendicular to the surface following a [111] direction, but then, eventually, other orientations⁴¹ are also found. The growth mode by MBE seems similar to that of Si(111) NWs,^{22,23} probably because the (111) surface is readily dislocated almost in the initial stages of growth and the subsequent Ge(111) growth is almost strain-free. In these first attempts, the Ge NWs are not very long because roughness induced by the FIB patterning limits the diffusion of material in this case, increasing nucleation sites between NWs. However, Ge nanostructures at the patterned sites are clearly seen in Figure 8b. The corresponding BS-SEM image (not shown) indicates the presence of Au only at the top of those nanostructures. Notice also that, in the absence of crawling effects, ordering by the patterns is quite effective.

Finally, turning back to the Si(001) case, we investigated the effect of the FIB ion dose on the morphological evolution of NW crawling. We note that the higher the ion dose, the wavier are the NWs (Figure 9). At low doses, the NWs are almost straight, with

Table 1. Evolution of the Mean Length and Cross Measure (Diameter) with the Ion Dose^a

ion dose (arb units)	mean length (nm)	mean diameter (nm)
1	1200 ± 100	52 ± 5
2	1100 ± 100	53 ± 5
2.5	1050 ± 100	53 ± 5
3	980 ± 100	47 ± 5
4	680 ± 100	44 ± 5

^aThe diameter is defined here as the square root of the NW section.

few kinks at 90° , whereas at high doses they are almost rolled up with a large density of kinks in the two [110] directions (see Figure 9d and e). This morphological evolution is not associated with any other relevant change, since both the NW total length and diameter remain rather constant (see Table 1) and the observed AuSi cluster size also remains constant. We attribute the waviness to kinking processes produced by interactions between NWs and substrate steps and kinks. Indeed, we have observed that, for a higher ion dose, the density of steps and kinks on the surface increases (associated with a higher rms roughness of the surface). According to the accepted models of epitaxial growth,⁴⁶ it can be argued that these sites will act as diffusion barriers, hindering the NWs from crossing those steps and kinks and producing the waviness. This is related to the Ehrlich–Schwoebel effect⁴⁷ found in other situations of epitaxial growth.

4. CONCLUSION

We have developed a three-step process based, first, on high-resolution mass-filtered FIB nanopatterning with gold ions, second, on formation during annealing of AuSi cluster catalysts, and, third, on nucleation and growth of Ge NWs starting from

the cluster catalysts. We show that the ion dose implanted near the patterns can be varied by changing the FIB experimental sputtering conditions. The latter also influences the subsequent density of AuSi clusters and their lateral distribution. During the MBE growth, Ge NWs nucleate on the AuSi clusters; they, first, grow almost perpendicular to the surface and rapidly kink and crawl along the [110] directions of the substrate. Following existing models, we explain the NW growth mechanism by the strain-driven evolution of the energy requested to create new facets at the trijunction between solid, liquid, and vapor. This energy includes surface energy and step edge energy, which both considerably evolve with strain. The strained NWs grow preferentially along the stepped surface at low misorientations from [001]. After strain relaxation, the step edge energy becomes large enough to impede further growth of the NW pedestal and produce the kinking of the NW and, subsequently, their crawling and the growth along [110] directions with equilibrium facets on their sides. The influence of the nanopatterns on the NW morphology is also exhibited: the larger is the surface roughness, the wavier are the NWs. The waviness is attributed to a larger density of kinks coming from interactions with surface steps and kinks produced during FIB patterning. The three-step process developed provides a promising way to investigate the processes of nucleation and growth of ordered arrays of NWs in various experimental situations.

■ AUTHOR INFORMATION

Corresponding Author

*E-mail: isabelle.berbezier@im2np.fr; isabel.alonso@icmab.es.

■ ACKNOWLEDGMENT

This work was supported by Spain's Ministry of Science and Innovation (MICINN) through Grants MAT2009-09480 (Project PIEZOHM) and CSD2010-00044 (Consolider NANOTHERM). I.C.M. is grateful to MICINN for a FPI fellowship and a mobility grant.

■ REFERENCES

- (1) Jung, J.-Y.; Guo, Z.; Jee, S.-W.; Um, H.-D.; Park, K.-T.; Moon, S. H.; Yang, J. M.; Lee, J.-H. *Nanotechnology* **2010**, *21*, 445303.
- (2) Stelzner, T.; Pietsch, M.; Andra, G.; Falk, F.; Ose, E.; Christiansen, S. *Nanotechnology* **2008**, *19*, 295203.
- (3) Alguno, A.; Usami, N.; Ujihara, T.; Fujiwara, K.; Sazaki, G.; Nakajima, K.; Shiraki, Y. *Appl. Phys. Lett.* **2003**, *83* (6), 1258–1260.
- (4) Lewis, N. S. *Science* **2007**, *315*, 798–801.
- (5) Wu, Y. Y.; Yang, P. D. *J. Am. Chem. Soc.* **2001**, *123*, 3165–3166.
- (6) Ge, S. P.; Jiang, K. L.; Lu, X. X.; Chen, Y. F.; Wang, R. M.; Fan, S. S. *Adv. Mater.* **2005**, *17*, 56–61.
- (7) Dailey, E.; Drucker, J. *J. Appl. Phys.* **2009**, *105*, 064317-1–064317-5.
- (8) Yan, H. F.; Xing, Y. J.; Hang, Q. L.; Yu, D. P.; Wang, Y. P.; Xu, J.; Xi, Z. H.; Feng, S. Q. *Chem. Phys. Lett.* **2000**, *323*, 224–228.
- (9) Zhang, R. Q.; Lifshitz, Y.; Lee, S. T. *Adv. Mater.* **2003**, *15*, 635–640.
- (10) Berbezier, I.; Ayoub, J. P.; Favre, L.; Ronda, A.; Morresi, L.; Pinto, N. *Surf. Sci.* **2011**, *605*, 7–11.
- (11) Wang, Y.; Schmidt, V.; Senz, S.; Gösele, U. *Nat. Nanotechnol.* **2006**, *1*, 186–189.
- (12) Chen, S. Y.; Chen, L. J. *Thin Solid Films* **2006**, *508*, 222–225.
- (13) Chen, C.-Y.; Wu, C.-S.; Chou, C.-J.; Yen, T.-J. *Adv. Mater.* **2008**, *20*, 3811–3815.
- (14) Peng, K. Q.; Hu, J. J.; Yan, Y. J.; Wu, Y.; Fang, H.; Xu, Y.; Lee, S. T.; Zhu, J. *Adv. Funct. Mater.* **2006**, *16*, 387–394.
- (15) Holmes, J. D.; Johnston, K. P.; Doty, R. C.; Korgel, B. A. *Science* **2000**, *287*, 1471–1473.
- (16) Yu, D. P.; Lee, C. S.; Bello, I.; Sun, X. S.; Tang, Y. H.; Zhou, G. W.; Bai, Z. G.; Zhang, Z.; Feng, S. Q. *Solid State Commun.* **1998**, *105*, 403–407.
- (17) Quitoriano, N. J.; Kamins, T. I. *Nanotechnology* **2011**, *22*, 065201.
- (18) Kamenev, B. V.; Sharma, V.; Tsybeskov, L.; Kamins, T. I. *Phys. Status Solidi* **2005**, *202* (14), 2753–2758.
- (19) Zhang, Y. F.; Tang, Y. H.; Peng, H. Y.; Wang, N.; Lee, C. S.; Bello, I.; Lee, S. T. *Appl. Phys. Lett.* **1999**, *75* (13), 1842–1844.
- (20) Kodambaka, S.; Hannon, J. B.; Tromp, R. M.; Ross, F. M. *Nano Lett.* **2006**, *6* (6), 1292–1296.
- (21) Dailey, E.; Madras, P.; Drucker, J. *Appl. Phys. Lett.* **2010**, *97*, 143106-1–143106-3.
- (22) McIntyre, P. C.; Adhikari, H.; Goldthorpe, I. A.; Hu, S.; Leu, P. W.; Marshall, A. F.; Chidsey, C. E. D. *Semicond. Sci. Technol.* **2010**, *25*, 024016.
- (23) Wolfsteller, A.; Geyer, N.; Nguyen-Duc, T.-K.; Das Kanungo, P.; Zakharov, N. D.; Reiche, M.; Erfurth, W.; Blumtritt, H.; Kalem, S.; Werner, P.; Gösele, U. *Thin Solid Films* **2010**, *518*, 2555–2561.
- (24) Schubert, L.; Werner, P.; Zakharov, N. D.; Gerth, G.; Kolb, F. M.; Long, L.; Gösele, U.; Tan, T. Y. *Appl. Phys. Lett.* **2004**, *84* (24), 4968–4970.
- (25) Kramer, A.; Boeck, T.; Schramm, P.; Fornari, R. *Physica E* **2008**, *40*, 2462–2467.
- (26) Molnar, W.; Lugstein, A.; Pongratz, P.; Auner, N.; Bauch, C.; Bertagnoli, E. *Nano Lett.* **2010**, *10*, 3957–3961.
- (27) Okamoto, H.; Massalski, T. B. In *Binary Alloy Phase Diagrams*; ASM International: Materials Park, OH, Vol. 1, 1990.
- (28) Nguyen, P.; Ng, H. T.; Meyyappan, M. *Adv. Mater.* **2005**, *17* (5), S49–S53.
- (29) Ross, F. M.; Tersoff, J.; Reuter, M. C. *Phys. Rev. Lett.* **2005**, *95*, 146104-1–146104-4.
- (30) Schmidt, V.; Senz, S.; Gösele, U. *Appl. Phys. A: Mater. Sci. Process.* **2005**, *80*, 445–450.
- (31) Dubrovskii, V. G.; Sibirev, N. V.; Cirlin, G. E.; Harmand, J. C.; Ustinov, V. M. *Phys. Rev. E* **2006**, *73*, 021603-1–021603-10.
- (32) Zakharov, N. D.; Werner, P.; Gerth, G.; Schubert, L.; Sokolov, L.; Gösele, U. *J. Cryst. Growth* **2006**, *290*, 6–10.
- (33) Williams, R. S.; Medeiros-Ribeiro, G.; Kamins, T. I.; Ohlberg, D. A. *A. J. Phys. Chem. B* **1998**, *102* (48), 9605–9609.
- (34) Fan, H. J.; Zacharias, M. *J. Mater. Sci. Technol.* **2008**, *24* (4), S89–S93.
- (35) Koto, M.; Marshall, A. F.; Goldthorpe, I. A.; McIntyre, P. C. *Small* **2010**, *6* (9), 1032–1037.
- (36) Schwarz, K. W.; Tersoff, J. *Phys. Rev. Lett.* **2009**, *102* (20), 206101-1–206101-4.
- (37) Schwarz, K. W.; Tersoff, J. *Nano Lett.* **2011**, *11*, 316–320.
- (38) Shenoy, V. B.; Freud, L. B. *J. Mechanics Physics Solids* **2002**, *50* (9), 1817–1841.
- (39) Tuinstra, F.; Scholte, P. M. L. O.; Rijnders, W. I.; van den Berg, A. J. *Surf. Sci.* **1994**, *317*, 58–64.
- (40) Lu, G.-H.; Cuma, M.; Liu, F. *Phys. Rev. B* **2005**, *72*, 125415-1–125415-6.
- (41) Pecora, E. F.; Irrera, A.; Artoni, P.; Boninelli, S.; Bongiorno, C.; Spinella, C.; Priolo, F. *Electrochem. Solid State Lett.* **2010**, *13*, K53–K55.
- (42) Woodruff, J. H.; Ratchford, J. B.; Goldthorpe, I. A.; McIntyre, P. C.; Chidsey, C. E. D. *Nano Lett.* **2007**, *7*, 16371642.
- (43) Aqua, J.-N.; Frisch, T. *Phys. Rev. B* **2010**, *82*, 085322-1–085322-13.
- (44) Motta, N.; Rosei, F.; Sgarlata, A.; Capellini, G.; Mobilio, S.; Boscherini, F. *Mater. Sci. Eng.* **2002**, *B88*, 264–268.
- (45) Vescan, L. *J. Phys.: Condens. Matter* **2002**, *14*, 8235–8252.
- (46) Venables, J. A. *Physica A* **1997**, *239*, 35–46.
- (47) Zhang, Z.; Lagally, M. G. *Science* **1997**, *276*, 377–383.